Journal of Applied Physics

RESEARCH ARTICLE | SEPTEMBER 26 2025

Results on re-verification tests of spent fuel casks with muon tomography: MUTOMCA project

Special Collection: Muography: Discoveries, Innovations, and Applications

P. Andreetto ; K. Aymanns ; M. Balling; M. Benettoni ; N. Bez ; G. Bonomi ; L. Castellani ; P. Checchia ; E. Conti ; J. Dackner ; F. Gonella ; A. Jussofie; A. Lorenzon ; F. Montecassiano ; M. Mosconi ; M. Murtezi ; J. Niedermeier ; I. Niemeyer ; J. Pekkarinen; A. Rigoni Garola ; D. Scarpa ; M. Stuke ; M. Turcato; G. Zumerle

J. Appl. Phys. 138, 124903 (2025)
https://doi.org/10.1063/5.0272975

Journal of Applied Physics ARTICLE pubs.aip.org/aip/jap

Results on re-verification tests of spent fuel casks with muon tomography: MUTOMCA project

Cite as: J. Appl. Phys. **138**, 124903 (2025); doi: 10.1063/5.0272975
Submitted: 27 March 2025 · Accepted: 22 July 2025 ·
Published Online: 26 September 2025

P. Andreetto,[1] K. Aymanns,[2] M. Balling,[3] M. Benettoni,[1] N. Bez,[1] G. Bonomi,[4] L. Castellani,[1] P. Checchia,[1,a)] E. Conti,[1] J. Dackner,[5] F. Gonella,[1] A. Jussofie,[3] A. Lorenzon,[1] F. Montecassiano,[1] M. Mosconi,[5] M. Murtezi,[5] J. Niedermeier,[6] I. Niemeyer,[2] J. Pekkarinen,[5] A. Rigoni Garola,[1] D. Scarpa,[7] M. Stuke,[3] M. Turcato,[1] and G. Zumerle[1]

AFFILIATIONS

[1]INFN Padova and Department of Physics and Astronomy University of Padova, Padova, Italy
[2]Forschungszentrum Jülich GmbH, Jülich, Germany
[3]BGZ Gesellschaft für Zwischenlagerung mbH, Essen, Germany
[4]Department of Mechanical and Industrial Engineering, University of Brescia, Brescia, Italy
[5]European Commission, Directorate-General for Energy, Luxembourg, Luxembourg
[6]Nuclear Technology, Technical University Munich, Garching, Germany
[7]INFN Laboratori Nazionali di Legnaro, Padova, Italy

Note: This paper is part of the Special Topic on Muography: Discoveries, Innovations, and Applications.

[a)]**Author to whom correspondence should be addressed:** paolo.checchia@pd.infn.it

ABSTRACT

The MUTOMCA (MUon TOMography for shielding CAsks) international project explores the suitability of cosmic muon tomography, a non-invasive and non-destructive imaging method, for the re-verification of loaded spent fuel casks. Such casks are stored in dedicated interim storage facilities under continuous containment and surveillance by international safeguards authorities using unattended monitoring equipment. In the hypothetical case of a temporary failure of these instruments, resulting in a loss of continuity of knowledge, a re-verification of the spent fuel to fulfill international safeguard obligations would be required. The project aims to demonstrate the ability of muon tomography, a non-invasive and non-destructive imaging method, to distinguish between dummy elements and spent fuel assemblies based on their different densities. For this purpose, an experimental detector system based on drift tube technology was designed, developed, constructed, and installed for a field test at a dry storage facility in Germany (Grafenrheinfeld, operated by BGZ). The test examined two CASTOR® V/19 casks: one loaded with a mixed configuration of dummy elements and spent fuel assemblies and the other exclusively with spent fuel assemblies. This was the first real data reconstruction with muon tomography performed in an interim storage facility.

I. INTRODUCTION

Nuclear power plants typically operate using uranium dioxide (UO_2) or mixed oxide (MOX) fuel, which is manufactured into pellets and stacked within zirconium-based cladding tubes. For a pressurized water reactor (PWR), these tubes, or fuel rods, are grouped together to form fuel assemblies with a squared section. Each assembly is approximately 4–5 m in height and 20×20 cm^2 in section, with variations in geometric dimensions and the number of rods depending on the specific reactor design. After completing their operational cycle in a reactor core, the spent fuel assemblies are removed and temporarily stored in cooling pools. This storage allows the decay heat generated by the radioactive material to decrease to a safe level. Once the heat falls below a specific threshold, the spent fuel assemblies can be loaded into specially designed casks, such as the CASTOR® V/19. These casks are engineered to ensure safe transport and storage of the spent fuel assemblies (Dual Purpose Casks, DPCs). The International

Atomic Energy Agency (IAEA)[1,2] and the European Atomic Energy Community (Euratom) enforce various technical checks at nuclear facilities to ensure compliance with legal obligations. These measures verify that nuclear facilities are not misused and that nuclear material is not diverted from peaceful purposes. Safeguards' implementation includes unattended containment and surveillance instrumentation, fundamental for maintaining Continuity of Knowledge (CoK), as well as the verification of nuclear material through destructive and non-destructive assay (DA and NDA) measurements. CoK ensures that information gathered during inspections (like the results of DA and NDA verifications) by IAEA and Euratom is preserved over time. CoK relies on continuous monitoring through containment and surveillance systems, maintaining a secure and verifiable chain of information. This approach ensures the integrity of the verification process and upholds international nuclear non-proliferation agreements. However, in the event of a temporary failure of these instruments leading to a loss of CoK, it would be necessary to re-verify the spent fuel contained within self-shielding casks to meet international safeguards' obligations. Loaded DPCs present a complex array of material densities and atomic numbers, posing challenges for traditional NDA methods due to their self-shielding.

In this context, cosmic muon tomography has emerged as a promising alternative. Muon tomography[3–7] is a non-destructive technique, derived from Particle Physics experiments, which can be employed to investigate the internal composition of inaccessible volumes. It exploits the natural flux of cosmic-ray muons that are naturally produced by primary cosmic rays impinging on the earth's atmosphere. Muons are highly penetrating particles capable of traversing large amounts of matter with limited absorption. Several applications and different techniques can profit from muon interaction with matter.[8] In particular, cosmic muons have been used to study the content of a spent fuel cask in a pioneer experiment conducted in 2016–2018,[9] and this application has been considered in several simulation studies.[10–15]

The MUTOMCA (MUon TOMography for shielding CAsks) project explores the application of muon tomography as a method for verifying spent fuel loaded into CASTOR® V/19 casks. Initiated by Forschungszentrum Jülich (Germany) in collaboration with INFN Padova (Italy) and BGZ Company for Interim Storage (Germany), with support from the European Commission, the project leverages detectors based on drift tube technology to accurately measure particle trajectories and muon positions.

Two large-area drift tube detectors have been developed, constructed, and successfully tested. These detectors constitute the core of the experimental apparatus. The setup enables the investigation of the cask internal contents through three distinct methodologies. The first is based on muon absorption,[16–18] which depends on the material density and thickness, as well as on the muon energy spectrum. A muon is considered absorbed if it is detected by the upstream chamber (positioned before the cask), with a direction pointing to the downstream chamber but is not detected by it within a defined coincidence time window.

The transmission technique,[4,19,20] widely used in muon imaging for archaeological and geophysical applications, can also be applied in this context.

The third method[5,21–23] exploits multiple Coulomb scattering (MCS), which occurs when muons traverse dense materials without being absorbed. This scattering results in a deviation from the original trajectory. Although the mean angular deviation is zero, the distribution's width is sensitive to the material properties. This technique requires accurate reconstruction of the muon path both before and after it passes through the cask. It provides information on a characteristic of the crossed material, which includes the atomic number and the density.

In this paper, we present the results obtained using the absorption-based method. The primary goal is to effectively differentiate between spent fuel assemblies and dummy elements (squared steel tubes with approximately the same mass as fuel assemblies) within specific loading configurations. This paper highlights the detector design (Sec. II), the measurement setup in a dedicated field test at the interim storage facility at Grafenrheinfeld in Germany (Sec. III), and presents the obtained results (Sec. IV).

II. THE DETECTOR

To meet budget constraints and reduce construction complexity, the detector was designed to cover only one-third of the cask surface at a time, achieving full coverage through a series of rotations. Software simulations confirmed the feasibility of this approach, as discussed below.

The MUTOMCA experimental detector system was developed with the specific characteristics of the CASTOR® V/19 cask in mind, which was chosen for testing. Given the large volume requiring inspection, a detector based on drift tube technology was selected.[24] This technology is cost effective for large-area detectors (>10 m^2) since it ensures good single point and track resolution with a relatively small number of cells, and it can use commercial material as aluminum tubes. Furthermore, a general concern about the possibility to reconstruct cosmic muon tracks in the vicinity of a DPC is due to the high radioactive background emitted by the cask. In a dedicated test conducted in 2018 at the Neckawestheim interim storage facility,[24] it was demonstrated that a prototype detector based on drift tube technology is able to reconstruct tracks even in the presence of such a background. However, given the large uncertainty of those measurements, the system was designed to cope with a higher background.

Our Drift Tubes (DT) are aluminum tubes, each 4.5 m long, 50 mm in diameter, and a wall thickness of 1.5 mm. The system consists of two detection modules, each made up of six layers of DTs.

Each tube functions as an individual detection cell. At its core, there is a coaxial Copper Beryllium (CuBe) wire with a diameter of 100 μm, which is tensioned to approximately 6 N to ensure alignment and stability. The ends of the tube are sealed with plastic caps that provide both mechanical closure and electrical contact with the wire. The detection system features a readout setup at each end of the wire. To ensure efficient operation, a 5 mm inlet pipe is used to allow the flow of the chosen gas mixture—85% Argon (Ar) and 15% Carbon Dioxide (CO_2). Given the gas tightness of the detector, a gas flow rate of 0.5 l/min, maintained with an overpressure of 4–5 hPa, is sufficient to maintain a negligible oxygen contamination (<100 ppm) and, hence, to ensure the detector's optimal

performance. The CuBe wire is connected to a 3000 V high-voltage supply, while the outer surface of each tube maintains a ground electrical contact, establishing a radial electric field within the tube. To minimize ambiguities in the reconstructed muon trajectory, a separation of 4.33 cm is introduced between the third and fourth layers of the detector modules. Each layer consists of 30 or 31 drift tubes, resulting in a total of 183 tubes per module and 366 tubes in the entire setup.

The double readout system at both ends of the wire in each tube enables high-precision measurements (330 μm) of the distance of the particle's trajectory from the wire, utilizing the drift time of ionization electrons.[24] Additionally, the system provides lower-precision longitudinal measurements (>20 cm) of the particle's position along the tube, calculated from the difference in signal arrival times at the two wire ends. This configuration allows for precise reconstruction of the muon track in the horizontal plane while providing a coarser estimate of its vertical position. Furthermore, the double readout ensures continuous drift time measurement even if one readout channel fails, preventing inefficiencies in the detector's operations. The DT modules were carefully designed, constructed, assembled, and instrumented by the INFN Padova team at the Laboratori Nazionali di Legnaro (LNL). The validation process conducted at LNL verified the detector system's reliability and functionality, ensuring that it was fully prepared for integration into the experimental setup.

As illustrated in Fig. 1, alongside the DT modules, two INFN muon detectors, known as Super Layers (SLs), originally constructed for other experiments,[25,26] were incorporated into the setup. These additions enable precise measurements of co-ordinates parallel to the DT wire directions (vertical plane). Each SL comprises four layers of 71 or 72 rectangular drift cells, with wires oriented orthogonally to those in the DTs. Like the DTs, the SLs are filled with the same gas mixture and are integrated into the shared gas system.

Due to their distinct cell structure and electric field configuration, the maximum drift time in DT's extends up to 1400 ns, while in the SLs, it is approximately 400 ns. Moreover, as detailed in Refs. 27 and 28, SLs provide highly precise timing information (within a few nanoseconds) for particle arrivals by leveraging linear combinations of the drift times recorded by muons traversing the four SL layers.

A. Electronics, trigger, and readout

The DT modules require $183 \times 2 \times 2 = 732$ front-end (FE) channels to amplify signals on both sides of the tubes. SLs require $286 \times 2 = 572$ FE channels for a total of 1304 channels. The total number of high-voltage (HV) channels is $366 + 572 = 938$ considering DT and SL, respectively. As summarized in Fig. 2, where all connection details are included, the trigger and data acquisition system exploit the Artix7 Field Programmable Gate Array (28 nm FPGA) and the Zynq UltraScale + System on Chip (16 nm SoC) from AMD/XILINX Technologies. The system is composed of (i) 24 TDC boards for time-to-digital conversion of the approximate 1300 FE channels; each board exposes 64 TDC instruments that exploit the deserialization circuitry available within each I/O structure of 28 nm FPGA used; Double Data Rate (DDR) processing of the FE input, combined with a 500 MHz deserialization clock, results in an LSB of 1 ns, adequate for the intrinsic resolution of the detectors. (ii) Four data acquisition (DAQ) boards for trigger signal processing and TDC readout of 512ch simultaneously, based on 16 nm SoC. (iii) One global trigger and timing control board (GTT) for global trigger processing and clock delivering, based on

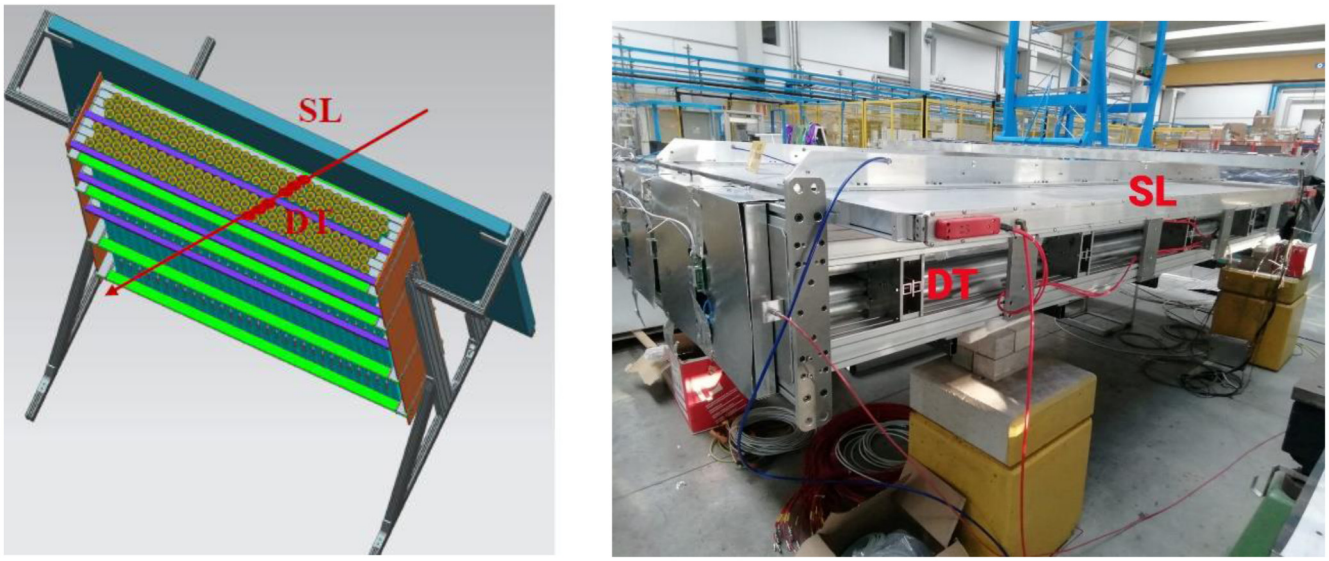

FIG. 1. Design of one detector module (left). Picture of one of the two detector modules assembled at LNL (right).

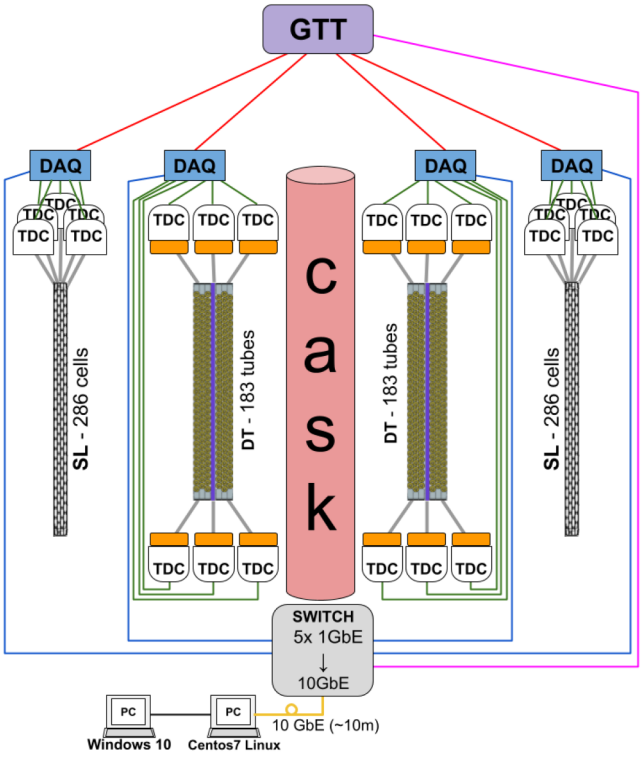

FIG. 2. Scheme of the electronics (DAQ and trigger). The gray connection between each TDC board and its detector represents a group of four Front-End flat ribbon cables for a total of 64 channels. The orange boxes represent the Feedthrough boards to the interface between the DT detector and TDC boards. The green lines leading from each DAQ board show the CAT6a[29] cables for delivering the clock to and reading data from each TDC board. Each red line represents a CAT6a cable delivering the clock and the serialized control signal to the DAQ board. In addition, one of the four twisted pairs included in the cable is used to send the trigger signal to the GTT board, which acts as the master trigger control. The magenta and blue lines represent CAT6a cables that implement a 1 GbE Ethernet physical layer, for controlling the GTT board and for reading out the DAQ board, respectively.

16 nm SoC, and (iv) 12 Feedthrough passive boards to interface between the detector and TDC boards.

The trigger system was designed on two levels to offer highly flexible logic:

(1) At the lower level, managed by one DAQ board, each sub-detector module, that is, any of the two DTs or two SLs, can send a trigger signal based on module-cell multiplicity and/or layer multiplicity with the ability to limit the count to a narrow number of nearby grouped cells. This ability, hereafter referred to as macro-cell implementation, is highly effective in reducing the trigger rate in the presence of an intense radioactive background that is expected to release uniformly distributed hits in the detector. To make the system even less sensitive to the radioactive background emitted by the cask, a hit filter capable of masking isolated hits that do not come from a muonic track was designed.
(2) At the highest level, managed by the GTT board, individual trigger signals from different DAQ modules can be freely combined according to the desired logic function to generate the global trigger signal.

FIG. 3. A picture of the complete muon detector assembled in Laboratori Nazionali di Legnaro.

Upon trigger activation, the entire event readout process is initiated and signals arriving within a time window of 2900 ns, sufficient to ensure full efficiency, are recorded. Data are transferred to the data acquisition PC with four dedicated 1 GbE Ethernet links (blue lines in Fig. 2). The prototypes for each type of board were thoroughly tested, and no issues were identified during the design and assembly phases. Furthermore, an accredited company performed electromagnetic interference (EMI) measurements for the detector and its electronic systems, as mandated by regulatory standards. The EN IEC 61000-6-4:2019 compliance certificate was successfully obtained.

Except for the analog FE board[30] housed inside the detector volume not depicted in Fig. 2—which is based on a customized ASIC designed by INFN—all electronics were built with commercial components and licenses, facilitating technology transfer in the industry.

B. Mechanical setup

The complete setup, including the SLs installed on the outer side of the DTs, is shown in Fig. 3. The support structure was designed and constructed to ensure high stability and to facilitate easy maneuvering of the entire system around the cask using a crane. To ensure precise positioning of the detector modules at the millimeter level and facilitate movement operations in the presence of a loaded CASTOR® V/19 cask, a support pad system has been devised. This system included support pads and tools, all housed within a hexagonal-shaped iron framework. It provided a reliable

method for efficiently and quickly moving the detector modules to the designated measurement positions, minimizing the time spent in proximity of the radioactive casks by all involved people.

C. Simulation

The MUTOMCA project was carefully planned by using a comprehensive system simulation tool. This approach enabled the detailed design of the detector modules and the creation of reconstruction algorithms without the need for initial real data. The simulations were instrumental in evaluating different data-taking setups, helping to determine the optimal geometric arrangement of the two detectors around the cask. This optimization aimed to minimize measurement time while enhancing the accuracy of image reconstruction.

The simulation package exploits the CERN GEANT4 toolkit[31] and was developed using the VMC framework[32] and the ROOT utilities.[33] The Monte Carlo simulation included a detailed model of the CASTOR® V/19 cask loaded with spent fuel, a realistic representation of the detector modules and their response to the passage of particles, and a reliable cosmic-ray muons generator, namely, the Eco-Mug[34] package.

D. Reconstruction methods

In this work, we use an image reconstruction algorithm based on muon absorption, which exploits the energy loss experienced by charged particles as they traverse matter. This energy loss is a function of both the material density and the path length traveled by the particle. Commonly referred to as the μCT algorithm,[18] this method enables the generation of a three-dimensional map of the average energy loss per unit length, also known as the stopping power (SP), which is directly correlated with the material density.

The algorithm operates by comparing the fraction of muons absorbed—measured by the two detector modules—with theoretical expectations derived from the path length of each muon and the energy spectrum of the incoming muons.

The output of the reconstruction is a three-dimensional grid of "voxels," namely, cubic pixels of homogeneous density.

III. THE FIELD TEST

After successful testing and validation at LNL, the detector modules and the support structure were transported to the storage facility at the Grafenrheinfeld site in Germany. In the third week of January 2023, the detector modules arrived and were placed in the reception area of the storage building, which is normally used for temporary holding of spent fuel casks prior to their transfer to the adjacent storage section.

All activities were carefully planned and conducted in accordance with ALARA (As Low As Reasonably Achievable) principles and the applicable dose limits for personnel. The experimental measurements were performed in the entrance and inspection area of the Interim Storage Facility, which is structurally separated from the storage area by thick concrete walls and shielding gates. The design and assembly of the experimental setup were completed within this shielded area. For each measurement, the cask was positioned at the experimental setup, and the gates to the storage area were securely closed. Further difficulties arose from the strict security requirements of the Interim Storage Facility and the influence this had on the selection and use of equipment. Only pre-approved devices meeting defined safety, security, and operational criteria could be brought into the facility. This necessitates further careful and detailed planning to ensure all measurement instruments and equipment complied with these constraints without compromising the experimental objectives.

After finalizing the experimental setup, the detector modules were powered on, and data collection commenced, initially without a spent fuel cask nearby for a preliminary period of a few days. Following this phase, a CASTOR® V/19 cask (serial number V/19 659 GP), which included 16 fuel elements and 3 dummy assemblies (referred to as C1), was brought over from the adjacent storage area and carefully positioned between the two detector modules as

	DET 0	DET 1
Pos 1	270°	90°
Pos 2	330°	150°
Pos 3	30°	210°

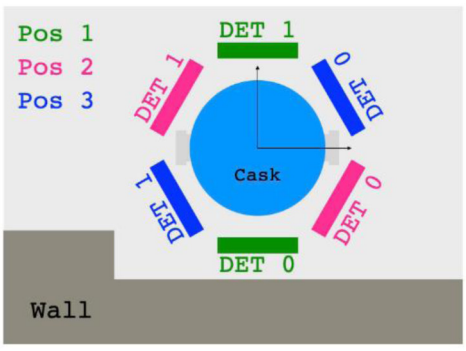

FIG. 4. Photo of the Grafenrheinfeld test installation with detector modules on both sides of CASTOR® V/19 (left). Overview of the detector module geometrical positioning (named, respectively, Pos 1, Pos 2, and Pos 3) during data taking (right).

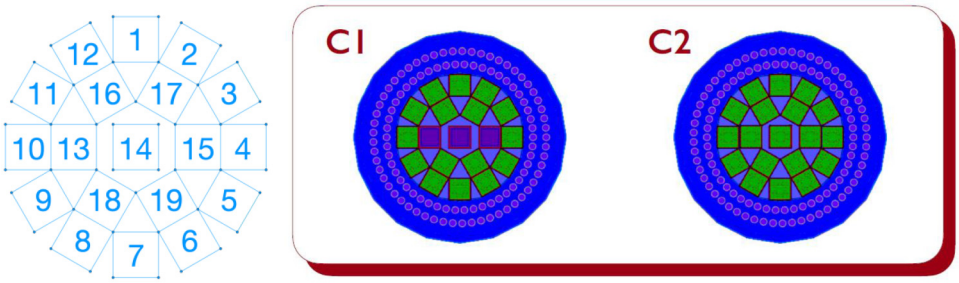

FIG. 5. Assembly numbering convention in CASTOR® V/19 casks (left). Draft of the two measured casks (right).

shown in Fig. 4 (left). Once the cask was positioned between the detector modules, it became evident that the background radiation from radioactive emissions was significantly higher compared to the 2018 measurements.[35] With C1 in place, the observed number of extra hits within the readout time window, not correlated with any muon track, was on average 11.7 ± 0.6 corresponding to a rate of 4.03 ± 0.21 MHz. This figure likely includes a minor contribution from electronic noise, estimated with data taken in rad-free conditions to be a few hits at most. The first cask, a mixed-loaded CASTOR® V/19, was then replaced by a fully loaded cask (serial number V/19 661 GP), containing only spent fuel assemblies (hereafter referred to as C2). With C2 in place, the average number of additional hits not correlated with muon tracks was 11.2 ± 0.9 (3.86 ± 0.31 MHz), a value comparable to what was observed with C1. It must be noticed that emitted radioactivity is not a good estimator of the absence of assemblies since it depends on general characteristics (radiation history, time elapsed from discharge) and relative disposition of the spent fuel assemblies. The entire data collection period extended from January 24th to February 24th, 2023. For C1, data were collected over 18 days, while for C2, the measurement lasted 11 days. In total, nearly one terabyte of data was acquired.

The radioactive background significantly impacted on the organization of the tests. It was decided to limit data collection to the three positions where the detector modules were placed at 180° excluding additional six positions with the detector modules placed at 120°, as foreseen in the original plan. While this decision was driven by necessity, it would inevitably affect the quality of the results, as discussed later. The three positions selected for data-taking are shown in Fig. 4 (right).

The modules were rotated by 60° each time using a crane, dividing the data collection into three separate datasets.

In Fig. 5 (left), the numbering convention for the assemblies of both casks is shown. The dummy elements in cask C1 correspond to number 13, 14, and 15 as depicted in Fig. 5 (right).

IV. TRIGGER AND DATASET

The setup described in Sec. III has two key implications for the trigger. First, muon tracks entering a SL module and pointing to the opposite module (DT or SL) do not cross more than three consecutive cells in any of the four layers. This allows the macro-cell implementation for SLs to be restricted to three cells. Similarly, muons entering a DT module and pointing to the opposite module do not cross more than eight consecutive cells in any of the six layers, which allows the macro-cell implementation for DTs to be restricted to eight cells. However, this implementation could not be applied to DTs in the case of modules placed at 120° (tracks can cross more than eight consecutive cells), which was one of the reasons data taking was not conducted in this configuration.

Despite these precautions, the background noise in the detector modules led to a modification in the trigger selection strategy to minimize unnecessary data recording on the storage disk. Specifically, in the absence of the cask, a logic OR of single submodules was preferred to capture any potential track crossing the most extensive detector area. This approach was viable, given that the total rate remained within a few kHz, with the requirement of at least 4 (3) layers with hits in DTs (SLs).

However, after introducing C1, the rate increased significantly, rising to over 60 kHz (Table I) and staying above 20 kHz for any detector pair included in the trigger. Additionally, due to the maximum drift time value and the need for precise timing information, the presence of at least one SL in the trigger became necessary. As a result, only two logic combinations of the four submodules (SL0, DT0, SL1, and DT1) were considered: (i) (SL0 && DT0 && DT1) || (SL1 && DT1 && DT0), also known as "AND3;" (ii) (SL0 && DT0) || (SL1 && DT1), known as "ORAND" (where "&&" represents the logical AND and "||" represents the logical OR). The AND3 configuration (10–20 Hz) requires a coincidence of three submodules, making it suitable for detecting muons that traverse the cask without being absorbed. It was used for short intervals to quickly assess data quality, as the rate of spurious triggers caused by occasional background signals is relatively low with this logic. On the other hand, the image reconstruction algorithm based on absorption requires the collection of muons that do not leave a signal on both sides of the cask. Therefore, the ORAND logic (<1 kHz) was employed for most of the data collection period. The data collection strategy during the field test was initially to gather data with C1 by moving the detector modules through the three positions. The

TABLE I. Trigger rates obtained in the absence and in the presence of a cask (C1) with two trigger logic combinations as discussed in the text.

	Rate (kHz)	
Trigger logic	Without cask	With cask
OR of single submodules	~2	~60
"ORAND"	~0.3	~0.6

detector was stationed at each position for at least one day, and the rotation was repeated twice. After this, C2 was installed, and a single rotation with at least 2 days spent at each position was performed. The ORAND configuration captures a high rate of background events, with at least one submodule registering events without muon tracks, as well as many muon events that do not point to the opposite detector. These events are, therefore, useless for both absorption and MCS algorithms. Useful events, which contained tracks, were selected using a full track reconstruction program, applied to both DTs and SLs. The fraction of useful tracks is typically at the percent level or lower.

All data were recorded and stored on the hard disks of two computers located in the test area behind a radiation shielding panel. The data were then transferred to a dedicated computer for quick analysis and subsequently uploaded to the Padova cloud center (*CloudVeneto*[36]).

V. DATA ANALYSIS AND TEST RESULTS

As mentioned earlier, a primary filter at the trigger level was implemented to mitigate the issues caused by the high radioactive background. Furthermore, during the final data analysis phase, an effective noise-cancellation strategy was employed to remove random hits from radioactive emissions that coincided with muon tracks.

The noise-cancelling strategy includes the following key components:

1. Time filter: This filter leverages the assumption that hits associated with a muon track occur within correlated time intervals, unlike hits caused by radioactive background, which are randomly distributed within the acquisition window. Given the requirement of having SL signals in the trigger logic, the precise time reconstruction and shorter drift time of the SL modules are particularly effective in excluding hits that do not match the expected arrival time of a muon track.
2. Space filter: This filter operates on the principle that hits from a muon track are spatially correlated, appearing in close proximity to one another. In contrast, noise hits tend to be isolated.
3. Clustering filter: This filter focuses on identifying the region of the detector with the highest density of hits. It identifies the main cluster of hits within the detector area, which is likely to correspond to a muon track, while disregarding smaller, isolated noise hits.

While the space filter proved to be highly effective in removing noise hits and aiding the cluster identification process, it was intentionally omitted from the final data reduction procedure to avoid introducing any inefficiencies in track detection. Instead, the noise cancellation relied primarily on the time and clustering filters to maintain a balance between noise rejection and accurate track reconstruction. Following the application of these filters, a Pattern Recognition process was used to detect and identify potential muon track candidates. Once a candidate track was identified, a Drift Time Fit algorithm was employed to refine the reconstruction by fitting the drift times of the hits and extracting the precise parameters of the muon track. Figure 6 provides a visual representation of a track candidate found by pattern recognition after noise filter and the subsequent track fitting for a typical event recorded during the field test. Tracks reconstructed with this procedure exhibit a position and angular resolution on the horizontal plane as accurate as expected.[24,37,38] However, the DT double readout is not adequate for providing precise information about the particle direction in the vertical plane (elevation angle), which was instead well measured by the SL modules. Nevertheless, the DT double readout proved to be very useful as it allowed the masking or removal of noisy channels and retaining information on at least one side for dead channels. This ensured that the appearance of dead zones could be avoided.

The muon tracks were independently reconstructed within the local reference frame of each detector module (DTs and SLs). Subsequently tracks were properly linked ensuring that hits from the DTs and SLs belong to the same particle. Following this correlation, a calibration process was performed to accurately determine the position and orientation of the detector modules around the cask. This calibration step was essential for aligning the modules relative to each other and the cask itself. Once calibrated, the tracks from each module were roto-translated into a global reference frame centered on the cask. This transformation allowed for a coherent and unified dataset, facilitating subsequent analysis and enabling precise tomographic reconstruction of the cask's internal structure.

The following selection criteria were implemented to filter events that are suitable for image reconstruction:

1. Reconstruction of ingoing tracks: Ingoing tracks must have a valid reconstruction from both the DT and SL modules. This

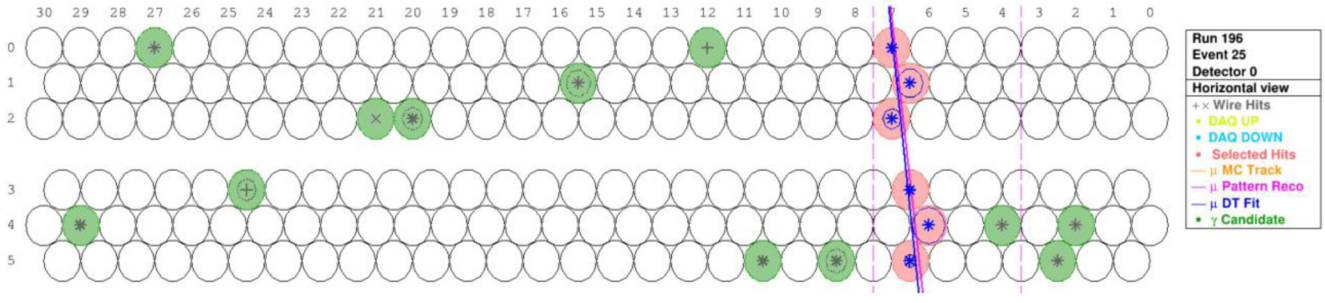

FIG. 6. Track candidate found by the Pattern Recognition step and reconstructed by the Drift Time fit.

requirement naturally follows from the conditions imposed by the ORAND trigger logic, which ensures that hits are recorded from both submodules.
2. Accurate timing information: Incoming tracks must have precise arrival times as determined by the SL modules. While not strictly mandatory, this criterion was introduced after it was observed that the DTs performed better when timing information was sourced from the SLs. This enhancement improves background noise rejection and provides a stronger constraint during the fit.
3. Track direction requirement: Incoming tracks must be directed toward the opposite detector module, ensuring that the muon can cross the entire system and consequently ensuring that the muon, if not absorbed, can be seen by the opposite detector.
4. Outgoing track verification: If the opposite SL module registers a track, it must be classified as an outgoing track. This check helps to distinguish between valid muon tracks and noise.
5. Time compatibility check: The muon arrival time recorded by the opposite module (if available) must be consistent with the arrival time of the ingoing track. This temporal consistency ensures that the correlated tracks originate from the same muon event.

These criteria are crucial for refining the dataset, focusing on high-quality events that contribute effectively to the tomographic image reconstruction process.

After the selection stage, the next step involves calculating the intersection points of the tracks with a virtual cylinder that encloses the cask. This cylinder defines the volume within which the image reconstruction will occur. The points where the ingoing tracks intersect the cylinder are termed as "entry points," while those where the outgoing tracks intersect are referred to as "exit points." These entry and exit points, along with their associated track directions, are fed into the Image Builder (IB) software as primary inputs. The IB software utilizes this information to reconstruct the internal structure of the cask, leveraging the directional data and the spatial co-ordinates of the track intersections.

The tomographic reconstruction software used in this study is based on analyzing the absorption of muons as they pass through the cask. When charged particles like muons travel through a medium, they gradually lose energy due to inelastic scattering with atomic electrons. If their initial energy is insufficient, they may eventually be stopped inside the material. The reconstruction method, known as the μCT algorithm,[18] has been described above.

The algorithm analyzes the muon paths using Line-of-Responses (LoRs), a term borrowed from PET tomography. LoRs represent the straight-line trajectories of muons through the material. Muons are subdivided into small samples of very close input position and direction. For each sample, the muons that do not have an exit point are classified as absorbed and the absorption fraction is computed. The expected fraction is also computed based on the muon momentum distribution and the stopping value (SP) in each voxel traversed by the muons of the sample. The software formulates a functional, which is a mathematical expression that sums up the squared differences between the observed and expected absorption fractions. By minimizing this functional changing the SP values assigned to each voxel, the algorithm estimates the best set of SP values of the material in each

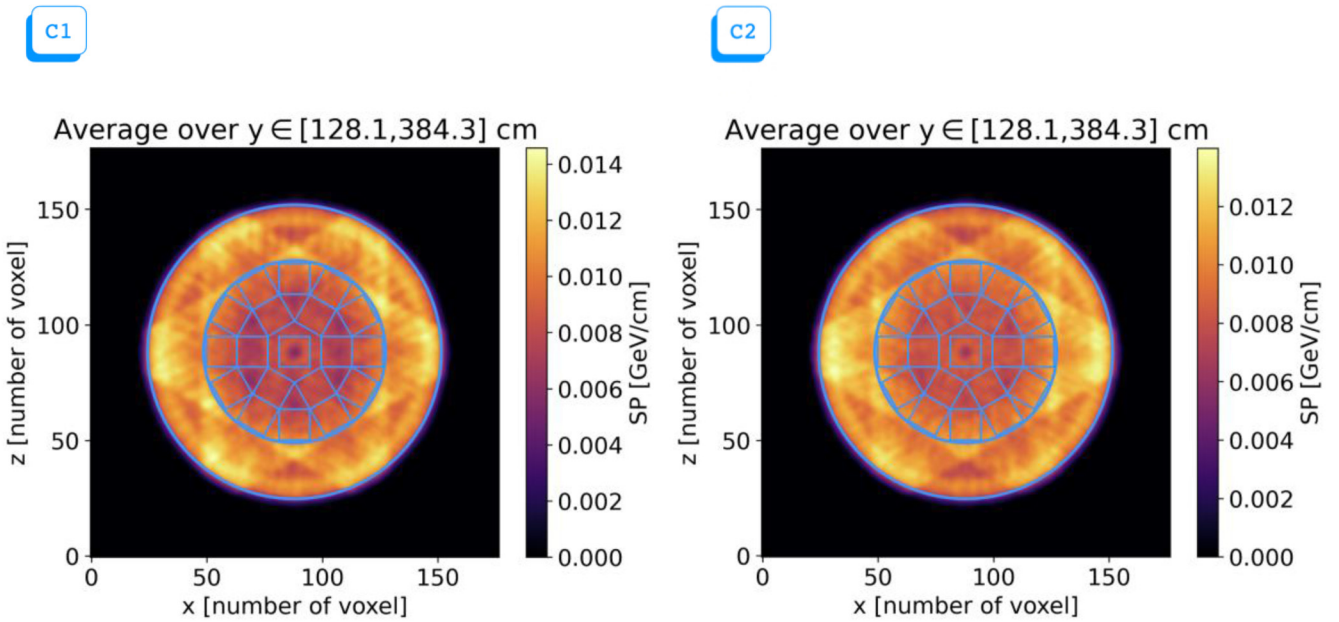

FIG. 7. Results of a μCT reconstruction of C1 and C2, horizontal view. The structure of the cask is represented in light blue. In this reconstruction, the voxel size is 1.83 cm.

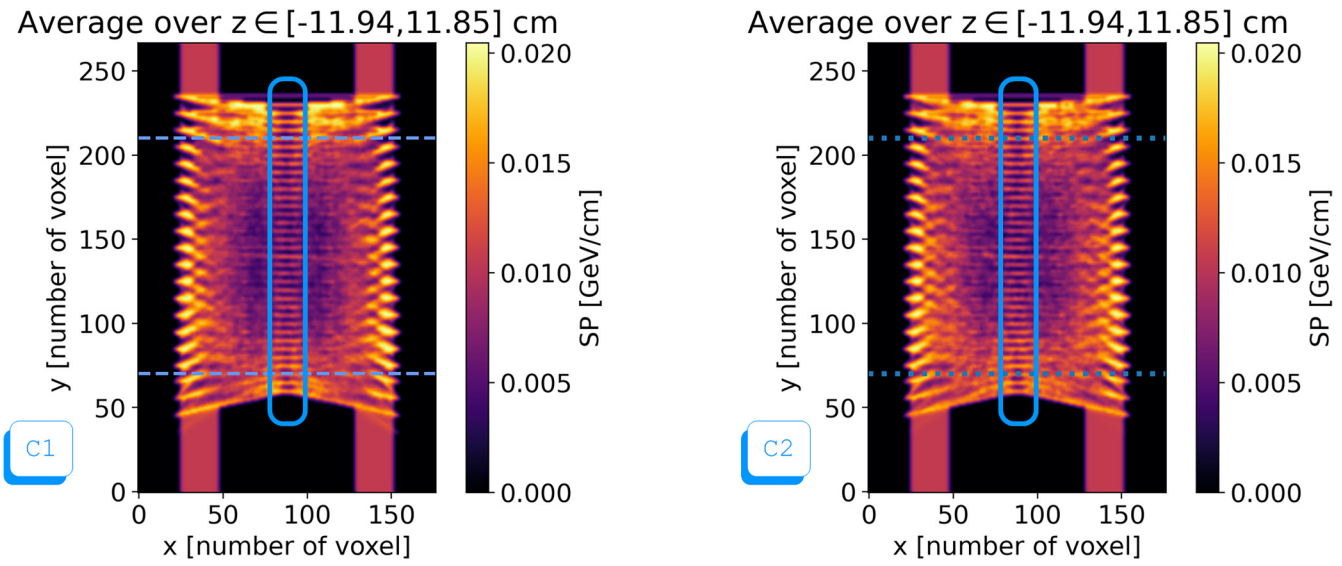

FIG. 8. Results of a μCT reconstruction of C1 and C2, vertical view. The central part of the cask features a reconstruction artifact, highlighted in blue, that spoils the reconstruction of assembly 14. The dashed horizontal lines correspond to the used vertical range as indicated in Fig. 7. In this reconstruction, the voxel size is 1.83 cm.

voxel within the imaging volume. The stopping power is directly related to the material density, allowing the algorithm to map out the internal structure of the cask.

In Fig. 7, the results of the μCT reconstruction for casks C1 and C2 are presented. The symmetry of the cask was leveraged to improve visualization by averaging the stopping power (SP) in the vertical direction. The vertical region where the SP average is considered extends by about 2 m in the region hosting assemblies. A grid overlay was applied to help distinguish the assembly structure within the cask.

Star-like artifacts appear in the outer part of the cask. They are due to muons that do not cross the outer detector because their direction was modified by multiple Coulomb scattering and are mistakenly classified as absorbed. This error is more frequent for muons pointing close to the border of the opposite detector, so producing the star shape of the anomaly. Additionally, another notable artifact, highlighted in Fig. 8, is evident near the axis of the reconstructed volume. This artifact[28] negatively impacts the accuracy of the assembly measurement for both C1 and C2. The intensity of these artifacts is exacerbated by the limited coverage of the CASTOR surface by the detectors. Moreover, their impact was further amplified due to the reduced number of data-taking positions, as previously discussed.

For this reason, in two of the following analyses to determine whether an assembly is real or dummy, the central assembly, number 14, is not included.

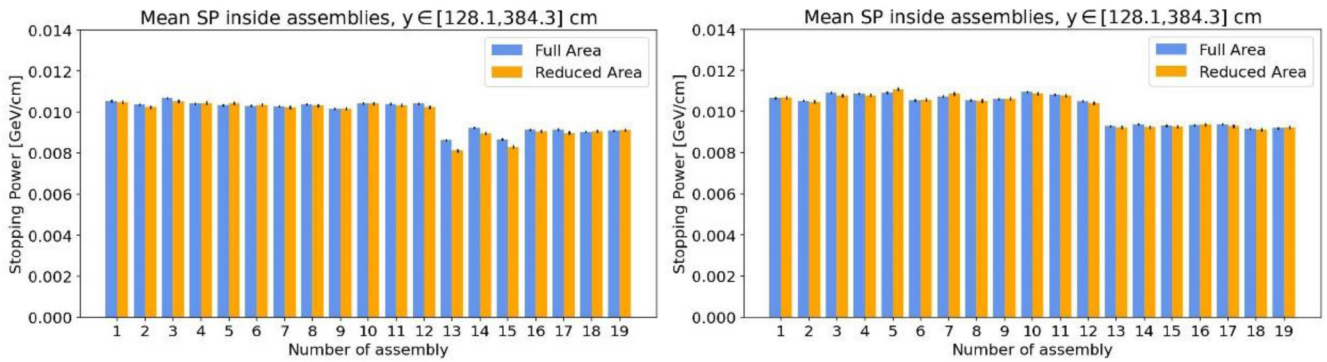

FIG. 9. Average value of the SP calculated inside the volume of the assemblies. The blue bars correspond to the SP calculated in the entire assembly volume, while the orange bars correspond to the SP calculated in the core of the assembly, i.e., using a reduced area. The small black segments on the top of the bars correspond to the uncertainty of the SP value.

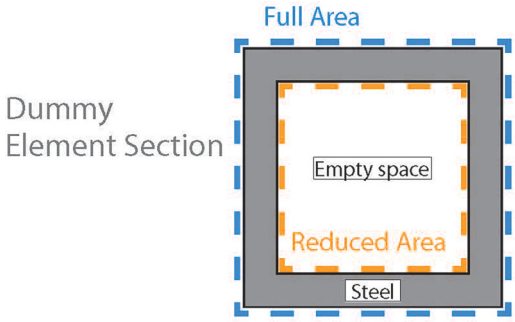

FIG. 10. Schematic representation of a dummy element (not to scale) showing the full area and the reduced area corresponding to the part filled with a lighter material.

Figure 9 presents histograms of the average stopping power (SP) measured in the voxels corresponding to the assembly volumes of the casks. A clear trend is observed where the SP values for the external assemblies are generally higher than those of the internal assemblies, a trend observed also with Monte Carlo simulation. However, in C1, assemblies 13 and 15 show significantly lower SP values compared to the other internal assemblies. In contrast, the SP values for these same assemblies in C2 are comparable to those of other internal assemblies.

Moreover, the structure of dummy elements as shown in Fig. 10 should be considered when calculating the average SP focusing only on the core of the assemblies. Using a smaller section to define their volume, the differences between the dummy elements and fuel assemblies should become more pronounced. This is because the inner part of the dummy elements is composed of a lighter material (air in the MC simulations), leading to a lower SP value compared to that of the denser fuel assemblies.

Three methods have been considered to differentiate between the two types of assemblies based on their SP measurements.

The first method to evaluate the deviation of two SP measurements, denoted by indexes i, j, is through compatibility, which is calculated as

$$\lambda_{ij} = \frac{|SP_i - SP_j|}{\sqrt{\sigma^2_{SP_i} + \sigma^2_{SP_j}}}, \tag{1}$$

with σ_{SP} being the uncertainty associated with the SP measurement. Defining a threshold value λ_{thr}, for $\lambda_{ij} \leq \lambda_{thr}$, the two measurements are considered to be compatible. Thus, taking a threshold $\lambda_{thr} = 3$, a value of $\lambda_{ij} \leq 3$ is expected when two assemblies of the same kind are compared, namely, two fuel assemblies or two dummy elements. Instead, when different kind of assemblies are compared, a value of $\lambda_{ij} > 3$ is expected. Figures 11 and 12 are a graphical representation of the compatibilities calculated between couples of internal assemblies of C1 and C2. As expected, in C2, all the measurements are compatible; in C1, measurements of assembly 13 and 15 are compatible with each other and incompatible with the rest of the internal assemblies. The SP measurements considered in Fig. 11 are obtained by taking the average of the SP in the entire volume of the assembly. The results obtained using the SP in the inner volume are shown in Fig. 12. As expected, the differences between the dummy elements and fuel assemblies become more pronounced.

The second method requires a comparison of the two casks. In this case, as shown in Fig. 13, compatibility is calculated without the absolute value in Eq. (1). Therefore, the compatibility interval is set to $-3 \leq \lambda_{ij} \leq 3$. As expected, all the SP measurements in the assemblies of C1 are compatible with the ones of C2, except for

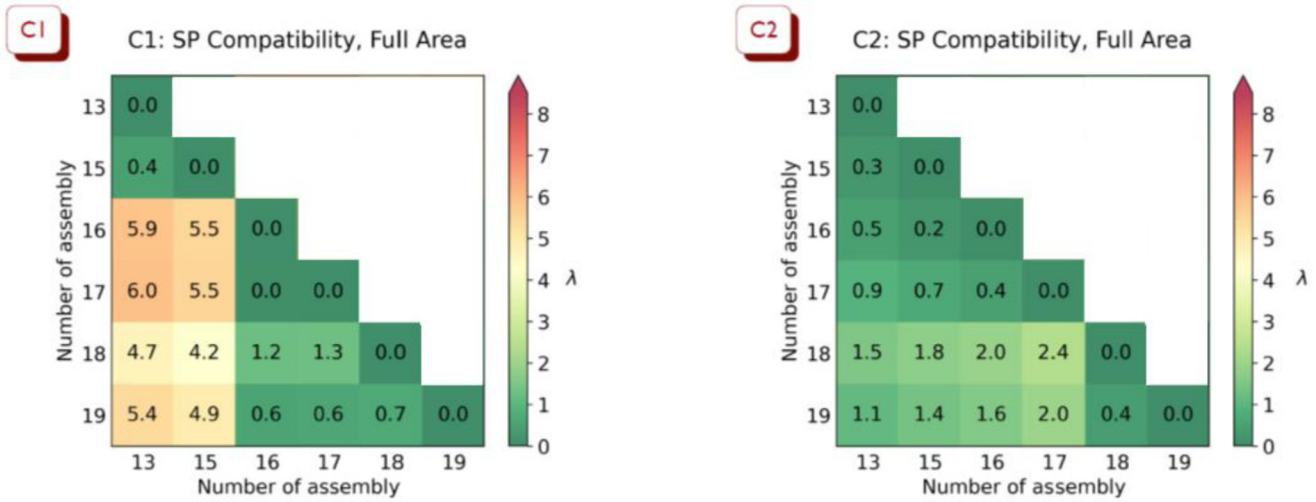

FIG. 11. Graphical representation of the compatibility calculated between couples of assemblies within the same cask. The color bar represents the compatibility value, which is also explicitly reported in each entry of this matrix. The average SP was calculated on the full assembly volume between SP measurements in the assemblies of C1 and C2.

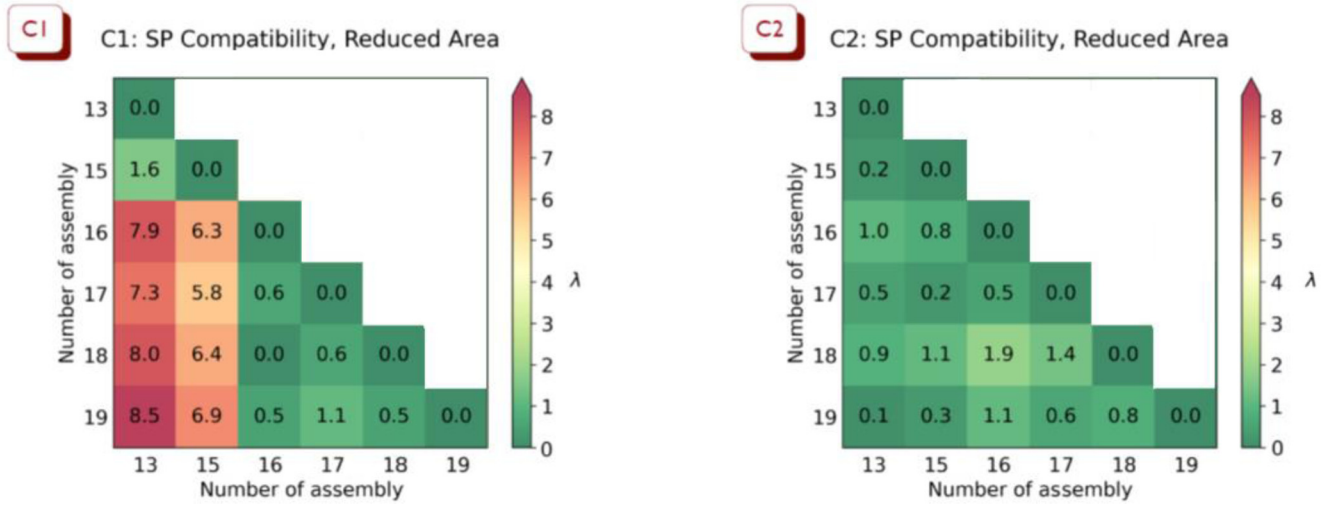

FIG. 12. Graphical representation of the compatibility calculated between the couples of assemblies within the same cask. The color bar represents the compatibility value, which is also explicitly reported in each entry of this matrix. The average SP was calculated on the reduced volume corresponding to the core of the assembly.

assemblies 13 and 15. The measurements of the SP in the core of the assembly volume exhibit a stronger deviation: as explained in case of Fig. 12, the inner part of dummy assemblies is filled with a lighter material, so the SP in that reduced area should be even smaller than that of fuel assemblies.

The third method relies, for each assembly, on the ratio between the average SP computed in the full area and the average computed in the reduced area. Since the inner area of dummy elements has a low density while the fuel assemblies are quite homogeneous, we expect values >1 for the former and ∼1 for latter ones. In detail, given

$$r_i = \frac{SP_{\text{ifull}}}{SP_{\text{ired.}}} \tag{2}$$

and considering the mean value m and the r.m.s. width σ of the r_i distribution extended to all the standard fuel assemblies, we obtain $m = 1.003$ and $\sigma = 0.008$ as shown in Fig. 14. The r_i values of the C1 dummy assemblies are all above the threshold $m + 3\sigma$, which is a further indication of the technology's ability to distinguish between the two types of assemblies. It is worthwhile noting that the deviation is present also for the central dummy assembly (C1 14) despite the abovementioned artifact.

Having more methods is undoubtably an advantage. It is out of scope of the present work to define a protocol to certify an alarm status (e.g., requiring two out of three indicators above a threshold), but the absence of false positives in all the proposed methods must be noticed. Nevertheless, the first and the third

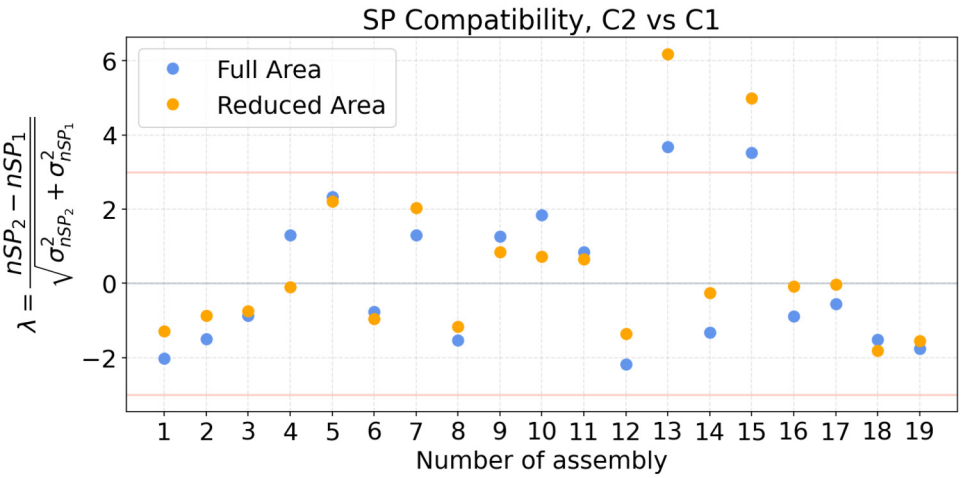

FIG. 13. Compatibility between SP measurements in the assemblies of C2 and C1. The three central assemblies are highlighted. Assembly 13 and 15 exhibit a compatibility value greater than 3, as expected when comparing two different kinds of assembly, while the measurement of assembly 14 is not reliable.

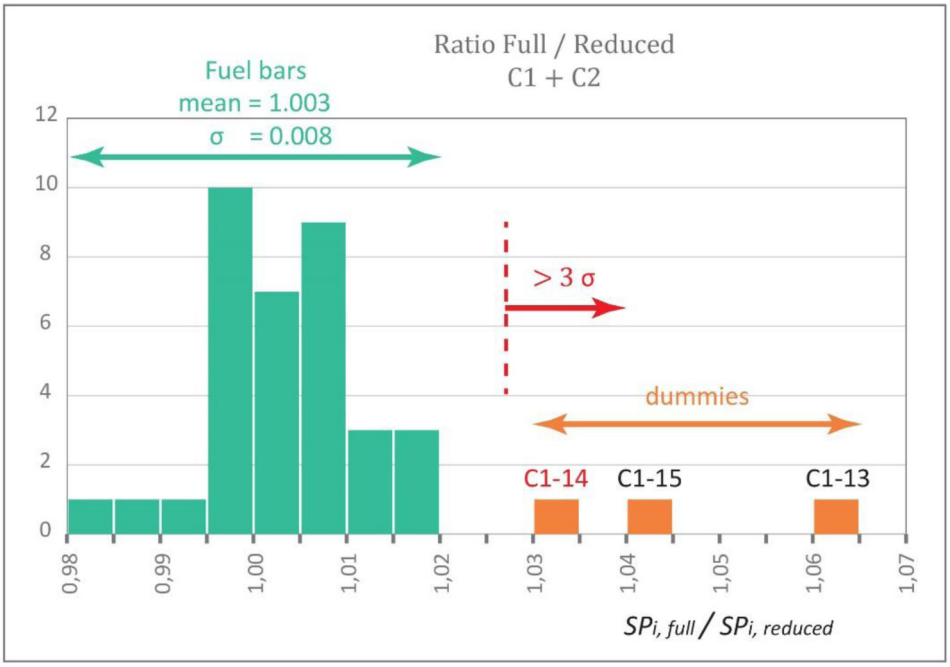

FIG. 14. Distribution of the r_i values for all fuel assemblies in C1 and C2 (green histogram). The entries corresponding to the dummy assemblies are presented in orange. They show incompatibility at the level of 3σ with respect to fuel assemblies.

methods do not require comparison with an additional cask, which can constitute an advantage.

VI. CONCLUSIONS

A particle detector based on drift tube technology was developed for the application of cosmic muon tomography to DPCs. A field test was conducted at the BGZ spent fuel interim dry storage facility in Grafenrheinfeld, aiming to examine the contents of two casks: one cask contained three dummy elements in the central positions and 16 fuel assemblies, replacing fuel assemblies, while the second was fully loaded with spent fuel assemblies.

To mitigate the impact on data acquisition and analysis of the background due to the cask radioactivity, several countermeasures were implemented. As a result, a substantial amount of useful muon track data was collected for both casks. The present experimental data have no precedent. In the past,[9] data were taken around a cask with empty slots that makes it much easier to recognize the absence of fuel assemblies. Dummy elements have approximately the same mass as a fuel assemblies, and hence, the distinction is much more difficult.

The collected data were processed at the INFN *CloudVeneto*[36] computer facility, where a muon absorption-based algorithm was applied to reconstruct images of the cask contents. A thorough evaluation of the algorithm's output, employing three distinct estimators to differentiate between fuel and dummy elements, demonstrated the effectiveness of the technology in detecting the presence of the dummy elements loaded in cask C1. Clear evidence for two out of the three dummy elements (assemblies 13 and 15) was found using the first two methods. The detection of the central dummy element (assembly 14) was affected by a notable reconstruction artifact near the axis of the reconstructed volume. This artifact negatively impacted the accuracy of the assembly measurement in that region, though the third method provided a fair indication for assembly 14. It is acknowledged that having multiple differentiation methods is an advantage, and the first and third methods do not require comparison with an additional cask.

This work highlights the potential of cosmic muon tomography as a viable tool for the re-verification of casks' contents. Additional analysis of the recorded data is planned to address unresolved issues, such as the reconstruction artifact, and improve the current results. This includes the implementation of the alternative image reconstruction method based on multiple Coulomb scattering, which is sensible also to the atomic number of the crossed material. These future efforts aim to enhance the accuracy and reliability of this technology for safeguard applications.

SUPPLEMENTARY MATERIAL

See the supplemental material for additional figures and tables concerning comparison with simulations.

ACKNOWLEDGMENTS

The MUTOMCA project was funded by the German Federal Ministry for the Environment, Nature Conservation, Nuclear Safety and Consumer Protection under the Funding Code No. 02W6279. A funding contribution and the support for detector transport to and from Germany was given by European Commission Directorate-General for Energy. CloudVeneto is acknowledged for the use of computing and storage facilities.

AUTHOR DECLARATIONS

Conflict of Interest

The authors have no conflicts to disclose.

Author Contributions

P. Andreetto: Software (equal). **K. Aymanns:** Funding acquisition (lead); Resources (lead); Writing – review & editing (equal). **M. Balling:** Resources (supporting). **M. Benettoni:** Validation (equal). **N. Bez:** Validation (equal). **G. Bonomi:** Conceptualization (equal); Software (equal). **L. Castellani:** Validation (equal). **P. Checchia:** Data curation (equal); Formal analysis (equal); Project administration (equal); Supervision (lead); Writing – original draft (lead). **E. Conti:** Methodology (supporting); Writing – review & editing (supporting). **J. Dackner:** Visualization (equal). **F. Gonella:** Data curation (lead); Validation (equal). **A. Jussofie:** Project administration (equal). **A. Lorenzon:** Formal analysis (lead); Software (equal); Writing – review & editing (equal). **F. Montecassiano:** Validation (equal). **M. Mosconi:** Funding acquisition (equal); Project administration (equal). **M. Murtezi:** Visualization (equal). **J. Niedermeier:** Data curation (supporting); Formal analysis (supporting). **I. Niemeyer:** Resources (equal). **J. Pekkarinen:** Visualization (equal). **A. Rigoni Garola:** Formal analysis (equal); Methodology (equal). **D. Scarpa:** Validation (equal). **M. Stuke:** Project administration (equal); Writing – review & editing (supporting). **M. Turcato:** Validation (equal). **G. Zumerle:** Formal analysis (equal).

DATA AVAILABILITY

The data that support the findings of this study are available from the corresponding author upon reasonable request.

REFERENCES

[1]International Atomic Energy Agency, IAEA, see https://conferences.iaea.org/event/150/contributions/5549/ for "Symposium on International Safeguards. Cosmic-ray Muography."

[2]international Atomic Energy Agency, see https://www.iaea.org/publications/15182/muon-imaging for "Muon Imaging" (2022).

[3]E. P. George, "Cosmic rays measure overburden of tunnel," Commonw. Eng. **42**(12), 455–457 (1955).

[4]L. W. Alvarez *et al.*, "Search for hidden chambers in the pyramids: The structure of the second pyramid of Giza is determined by cosmic-ray absorption.," Science **167**(3919), 832–839 (1970).

[5]K. R. Borodzin *et al.*, "Radiographic imaging with cosmic-ray muons," Nature **422**, 277 (2003).

[6]L. Bonechi, R. D'Alessandro, and A. Giammanco, "Atmospheric muons as an imaging tool," Rev. Phys. **5**, 100038 (2020).

[7]G. Bonomi *et al.*, "Applications of cosmic-ray muons," Prog. Part. Nucl. Phys. **112**, 103768 (2020).

[8]See a quite comprehensive list on *Cosmic Ray Muography*, edited by P. Scampoli and A. Ariga (World Scientific Publishing, 2023).

[9]J. M. Durham *et al.*, "Verification of spent nuclear fuel in sealed dry storage casks via measurements of cosmic-ray muon scattering," Phys. Rev. Appl. **9**, 044013 (2018).

[10]J. Gustafsson, "Tomography of canisters for spent nuclear fuel using cosmic-ray muons," M.S. thesis No. UPTEC F05 077 (Uppsala University, 2005).

[11]M. Österlund *et al.*, in *Tomography of Canisters for Spent Nuclear Fuel PoS (FNDA2006) 030* (Sissa Medialab, 2006), available at https://doi.org/10.22323/1.025.0030.

[12]G. Jonkmans *et al.*, "Nuclear waste imaging and spent fuel verification by muon tomography," Ann. Nucl. Energy **53**, 267–273 (2013).

[13]S. Chatzidakis, C. K. Choi, and L. H. Tsoukalas, "Analysis of spent nuclear fuel imaging using multiple Coulomb scattering of cosmic muons," IEEE Trans. Nucl. Sci. **63**, 2866–2874 (2016).

[14]D. Poulson *et al.*, "Cosmic ray muon computed tomography of spent nuclear fuel in dry storage casks," Nucl. Instrum. Methods Phys. Res. A **842**, 48–53 (2017).

[15]C. Park *et al.*, "Design and characterization of a muon tomography system for spent nuclear fuel monitoring," Nucl. Eng. Technol. **54**(2), 601–607 (2022).

[16]S. Procureur, "Muon imaging: Principles, technologies and applications," Nucl. Instrum. Methods Phys. Res. A **878**, 169–179 (2018).

[17]P. Checchia, Principle of Cosmic Muography-Techniques and Review, Chap. 3 of Ref. 8.

[18]S. Vanini *et al.*, "Muography of different structures using muon scattering and absorption algorithms," Philos. Trans. R. Soc., A **377**, 20180051 (2019).

[19]N. Lesparre *et al.*, "Geophysical muon imaging: Feasibility and limits," Geophys. J. Int. **183**(3), 1348–1361 (2010).

[20]K. Morishima, M. Kuno, A. Nishio, N. Kitagawa, Y. Manabe, M. Moto *et al.*, "Discovery of a big void in Khufu's pyramid by observation of cosmic-ray muons," Nature **552**, 386 (2017).

[21]L. J. Schultz *et al.*, "Image reconstruction and material Z discrimination via cosmic ray muon radiography," Nucl. Instrum. Methods Phys. Res., Sect. A **519**, 687–694 (2004).

[22]L. Schultz *et al.*, "Statistical reconstruction for cosmic ray muon tomography," IEEE Trans. Image Process. **16**(08), 1985–1993 (2007).

[23]M. Benettoni *et al.*, "Noise reduction in muon tomography for detecting high density objects," J. Instrum. **8**, P12007 (2013).

[24]P. Checchia *et al.*, "Muon tomography for dual cask purpose (MUTOMCA) project," in *Proceedings of Joint INMM/ESARDA Annual Meeting* (Institute of Nuclear Materials Management, 2021), see https://resources.inmm.org/sites/default/files/2021-09/a1673.pdf

[25]S. Chatrchyan *et al.*, "The CMS experiment at the CERN LHC," J. Instrum. **3**, S08004 (2008).

[26]M. Aguilar-Benitez *et al.*, "Construction and test of the final CMS barrel drift tube muon chamber prototype," Nucl. Instrum. Methods Phys. Res., Sect. A **480**, 658 (2002).

[27]M. De Giorgi *et al.*, Design and Simulations of the Trigger Electronics for the CMS Muon Barrel Chambers CMS TN/95-01.

[28]A. Lorenzon, "Addressing contemporary challenges with muography," Ph.D. thesis (University of Padova, 2024), available at https://hdl.handle.net/11577/3556440.

[29]See https://www.anixter.com/content/dam/Suppliers/Leviton/Brochures/Leviton%20-Cat6A%20Reference%20Guide.%20051518pdf.pdf for CAT6a cables.

[30]F. Gonella and M. Pegoraro, see https://cds.cern.ch/record/529411 for "'The MAD,' a Full Custom ASIC for the CMS Barrel Muon Chambers Front End Electronics."

[31]S. Agostinelli *et al.*, "Geant4—A simulation toolkit," Nucl. Instrum. Methods Phys. Res., Sect. A **506**, 250–303 (2003).

[32]See https://vmc-project.github.io/ for vmc project.

[33]R. Brun and F. Rademakers, "ROOT—An object oriented data analysis framework," Nucl. Instrum. Methods Phys. Res., Sect. A **389**, 81–86 (1997).

[34]D. Pagano *et al.*, "Ecomug: An efficient COsmic MUon generator for cosmic-ray muon applications," Nucl. Instrum. Methods Phys. Res., Sect. A **1014**, 165732 (2021).

[35]D. Ancius *et al.*, "Modelling of safeguards verification of spent fuel dry storage containers using muon trackers," in *Proceedings of the 41st ESARDA Annual Meeting, Stresa* (Publications Office of the European Union, 2019), p. 141, see https://esarda.jrc.ec.europa.eu/publications/2019-esarda-symposium-41st-esarda-annual-meeting_en.

[36]See https://cloudveneto.it for Cloud Veneto.

[37]A. Lorenzon *et al.*, in *INMM & Esarda Joint Annual Meeting, 22–26 May 2023* (Institute of Nuclear Materials Management, Vienna, 2023), available at https://resources.inmm.org/sites/default/files/2023-07/finalpaper_432_0512060054.pdf.

[38]G. Bonomi *et al.*, "Muon tomography for reverification of spent fuel casks (the MUTOMCA project)," J. Adv. Instrum. Sci. **2024**(1), 497 (2024).